Cosmic Consequences from the CMB, Circa Summer 96

J. Richard Bond

Canadian Institute for Advanced Research Cosmology Program

Canadian Institute for Theoretical Astrophysics, Toronto, Ontario, Canada

October 28, 1997

Abstract

A long-standing goal of theorists has been to constrain cosmological parameters that define the structure formation theory from CMB anisotropy experiments and large scale structure observations. The current status and future promise of this enterprise is described. We rightly celebrate Princeton's pivotal role in all this, over a full eighth of its venerable age, from background detection through tight distortion constraints, from the downward march in $\Delta T/T$ limits to discovery at large angles, then small, punctuated by decades of seminal theory, a MAP in the near-future and undoubtedly much beyond. Current band-powers in ℓ-space are consistent with a ΔT flat in frequency and broadly follow inflation-based expectations, but may still include residual signals. That their levels are $\sim (10^{-5})^2$ provides strong support for the gravitational instability theory, while the FIRAS constraints on energy injection rule out cosmic explosions as a dominant source of large scale structure. Band-powers at $\ell \gtrsim 200$ suggest the universe could not have reionized too early. To get the large scale structure of COBE-normalized fluctuations right provides encouraging support that the initial fluctuation spectrum was not far off the scale invariant form that inflation models prefer, $n_s = 1.0 \pm 0.2$ for DMR only, 1.1 ± 0.1 for DMR plus the Princeton SK95 experiment, flatter for open models. The CMB alone does not currently give powerful constraints on Λ and Ω_{tot}, but theoretical forecasts of future long duration balloon and satellite experiments are shown which predict percent-level accuracy among a large fraction of the 10+ parameters characterizing the cosmic structure formation theory, at least if it is an inflation variant.

1 The Theoretical Agenda

1.1 Early Universe Physics

The source of fluctuations to input into the cosmic structure formation problem (e.g., [1]) is likely to be found in early universe physics. We want to measure the CMB (and large scale structure) response to these initial fluctuations. The goal is the lofty one of peering into the physical mechanism by which the fluctuations were generated, by learning: the statistics of the fluctuations, whether Gaussian or non-Gaussian; the mode, whether adiabatic or isocurvature scalar perturbations, and whether there is a significant component in gravitational wave tensor perturbations; the power spectra for these modes (albeit over only 3 decades in wavenumber for CMB probes, Fig. 1, and fewer for large scale structure (LSS) probes).

The contenders for fluctuation generation mechanisms are (1) "zero point" oscillations in scalar and tensor fields that must be there in the early universe if quantum mechanics is applicable and (2) topological defects which may arise in the inevitable phase transitions expected in the early universe. Defects are described elsewhere in these proceedings.

1.2 Inflation

For quantum oscillations to be important, a period of accelerated expansion seems essential, for then the comoving Hubble length $(Ha)^{-1}$ shrinks in size, freezing the time-incoherent noise into time-coherent patterns for structure formation. Acceleration (i.e., inflation) seems to be generic unless it is explicitly forbidden by some law of physics unknown at this time. It may be extremely improbable *a priori* that a bit of space would accelerate and yet be highly probable *a posteriori* that we would find ourselves in a region that once inflated because of the vast space created. A major challenge for inflation models is a "natural" explanation of why post-inflation fluctuations should be $\sim 10^{-5}$ in size, as revealed by COBE and also LSS observations.

Many variants of the basic inflation theme have been proposed, sometimes with radically different consequences for the appearance of the CMB sky, which is used in fact to highly constrain the more baroque models. A rank-ordering of inflation possibilities: (1) adiabatic curvature fluctuations with nearly uniform scalar tilt over the observable range, slightly more power

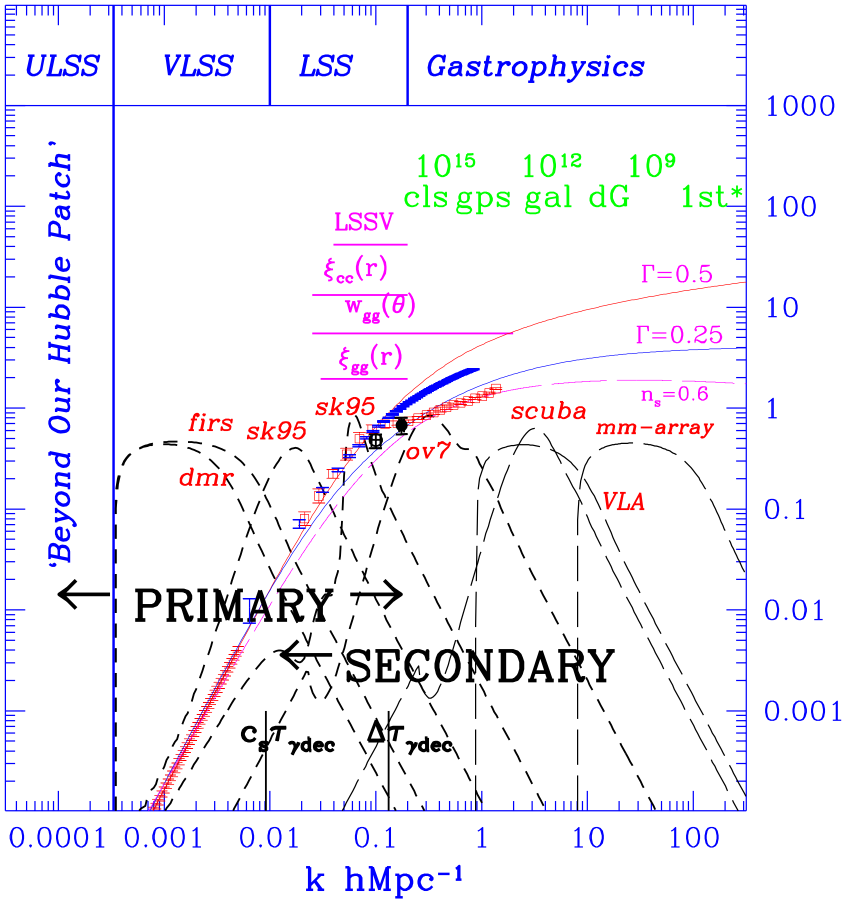

Figure 1: The bands in comoving wavenumber probed by CMB primary and secondary anisotropy experiments and by large scale structure observations are contrasted. Sample (linear) density power spectra (actually $[d\sigma_\rho^2/d\ln k]^{1/2}$) are plotted for the "standard" $n_s = 1$ CDM model (labelled $\Gamma = 0.5$), a tilted ($n_s = 0.6$, $\Gamma = 0.5$) CDM model and for a model with the shape modified ($\Gamma = 0.25$) by changing the matter content of the Universe. The hatched region at low k gives the 4 year DMR error bars. The solid data point in the cluster-band denotes the constraint from the abundance of clusters, and the open data point at $10\,h^{-1}$ Mpc a constraint from streaming velocities (for Ω_{tot}=1,Ω_{vac}=0). The open squares are an estimate of the linear power spectrum from current galaxy clustering data by Peacock (1996), while the error bars are samples of how well the Sloan Digital Sky Survey is expected to do (Vogeley and Szalay 1996). A bias is "allowed" to (uniformly) raise the shapes to match the observations. The width of the CMB photon decoupling region and the sound crossing radius ($\Delta\tau_{\gamma dec}, c_s\tau_{\gamma dec}$) are also shown.

to large scales ($n_s < 1$) than "scale invariance" ($n_s = 1$) gives, a predictable nonzero gravity wave contribution with tilt similar to the scalar one, and tiny mean curvature ($\Omega_{tot} \approx 1$); (2) same as (1), but with a tiny gravity wave contribution; (3) same as (1) but with a subdominant isocurvature component of nearly scale invariant tilt (the case in which isocurvature dominates is ruled out); (4) radically broken scale invariance with weak to moderate features (ramps, mountains, valleys) in the fluctuation spectrum (strong ones are largely ruled out); (5) radical breaking with non-Gaussian features as well; (6) "open" inflation, with quantum tunneling producing a negatively-curved (hyperbolic) space which inflates, but not so much as to flatten the mean curvature ($d_c \sim (Ha)^{-1}$, not $\gg (Ha)^{-1}$, where $d_c \equiv H_0^{-1}|1 - \Omega_{tot}|^{-1/2}$); (7) quantum creation of compact hyperbolic space from "nothing" with volume d_T^3 which inflates, with $d_T \sim (Ha)^{-1}$, not $\gg (Ha)^{-1}$, and d_T of order d_c; (8) flat ($d_c = \infty$) inflating models which are small tori of scale d_T with d_T a few $(Ha)^{-1}$ in size. It is quite debatable which of the cases beyond (2) are more or less plausible, with some claims that (4) is supersymmetry-inspired, others that (6) is not as improbable as it sounds (Gott, these proceedings). It is the theorists' job to push out the boundaries of the inflation idea and use the data to select what is allowed.

1.3 Cosmological Hydrodynamics

Although hydrodynamic and radiative processes are expected to play important roles around collapsed objects and may bias the galaxy distribution relative to the mass (*gastrophysics* regime in Fig. 1), a global role in obscuring the early universe fluctuations by late time generation on large scales now seems unlikely. Not too long ago it seemed perfectly reasonable based on extrapolation from the physics of the interstellar medium to the pregalactic and intergalactic medium to suppose hydrodynamical amplification of seed cosmic structure would obscure primordial fluctuations from the early Universe. The strong limits on Compton cooling from FIRAS [4], in energy $\delta E_{Compton\ cool}/E_{cmb} = 4y < 6.0 \times 10^{-5}$ (95% CL), constrain the product $f_{exp} R_{exp}^2$ of filling factor f_{exp} and bubble formation scale R_{exp}, to values too small for a purely hydrodynamic origin. If supernovae were responsible for the blasts, the accompanying presupernova light radiated would have been much in excess of the explosive energy (more than a hundred-fold), leading to much stronger restrictions e.g., [1].

1.4 Cosmic Parameters

Even simple Gaussian inflation-generated fluctuations for structure formation have a large number of early universe parameters we would wish to determine: power spectrum amplitudes at some normalization wavenumber k_n for the modes present, $\{\mathcal{P}_s(k_n), \mathcal{P}_{is}(k_n), \mathcal{P}_{GW}(k_n)\}$; shape functions for the "tilts" $\{\nu_s(k), \nu_{is}(k), \nu_t(k)\}$, usually chosen to be constant or with a logarithmic correction, e.g., $\nu_s(k_n), d\nu_s(k_n)/d\ln k$. (The scalar tilt for adiabatic fluctuations, ν_s is related to the usual index, n_s, by $\nu_s = n_s - 1$.) The transport problem is dependent upon physical processes, and hence on physical parameters. A partial list includes the Hubble parameter h, various mean energy densities $\{\Omega_{tot}, \Omega_B, \Omega_{vac}, \Omega_{cdm}, \Omega_{hdm}\}\mathrm{h}^2$, and parameters characterizing the ionization history of the Universe, e.g., the Compton optical depth ζ_C from a reheating redshift z_{reh} to the present. The density in relativistic neutrinos (and decaying particle products, if any), the abundance of primordial helium, etc. should also be considered as parameters to be determined. The count is thus at least 17, and even if an isocurvature contaminant (i.e., § 1.2 (3)) is dropped as too baroque, 15+ remain. Estimates of errors on a smaller 9 parameter inflation set for the MAP and COBRAS/SAMBA satellites are given in § 2.5.

For a given model, the early universe power spectrum amplitude measures are uniquely related to late-time power spectrum measures of relevance for the CMB, such as the quadrupole or bandpowers for various experiments, or to large scale structure observations, such as the *rms* density fluctuation level on the $8\,\mathrm{h}^{-1}$ Mpc (cluster) scale, σ_8, so these could be used in place of the primordial power amplitudes.

In inflation, the ratio of gravitational wave power to scalar adiabatic power is $\mathcal{P}_{GW}/\mathcal{P}_s \approx (-4\nu_t)/(1-\nu_t/2)$. This could lower the parameter count by one, except there are small corrections. The tensor tilt is related to the deceleration parameter q of the Universe during inflation by $\nu_t/2 \approx 1 + q^{-1}$ plus small corrections. In [5] we took two cases, with $\nu_t = 0$ and thus no gravity wave contribution (for nearly critical acceleration, $q \approx -1$, as in natural inflation), and with $\nu_t = \nu_s$ if the scalar tilt is negative (subcritical but nearly uniform acceleration) and ν_t=0 if the scalar tilt is positive.

The arena in which theory battles observation is the anisotropy power spectrum, e.g., Fig. 2 and Fig. 4.

In § 2.2,2.3, constraints Andrew Jaffe and I [5] have obtained using 4 year

DMR [6], SP94 [7] and SK94/SK95 [8, 9] data sets in the parameter space $\{t_0, \mathrm{h}, \Omega_{tot}, \Omega_B \mathrm{h}^2, \Omega_{vac}, \Omega_{hdm}, \Omega_{cdm}, \nu_s, \nu_t, \sigma_8\}$ are described. The age of the Universe is t_0; ht_0 is a function of $\{\Omega_{vac}, \Omega_{tot}\}$, so one parameter is redundant. (We assumed reheating occurred sufficiently late to have a negligible effect on $\mathcal{C}_\ell$, by no means clear.) With current errors on the data, this space is too large for effective parameter estimation. Instead we restricted our attention to various subregions, such as $\{\sigma_8, n_s, \mathrm{h} \,|\, \mathrm{fixed}\, t_0, \Omega_B \mathrm{h}^2\}$, where $\Omega_{tot} = 1$ and Ω_{vac} is a function of ht_0. The t_0's we chose were 11, 13, 15 Gyrs. A recent estimate for globular cluster ages is $14.6^{+1.7}_{-1.6}$ Gyr [10]. Usually we chose the "standard" nucleosynthesis estimate $\Omega_B \mathrm{h}^2 = 0.0125$, but we also let $\Omega_B \mathrm{h}^2$ vary, over the range $0.003125 \leq \Omega_B \mathrm{h}^2 \leq 0.05$ for the $\Omega_{vac} = 0$ case. (A sample of a restricted parameter sequence is shown in Fig. 4.) We constrained $0.5 \leq n_s \leq 1.5$, $0.43 \lesssim \mathrm{h} \leq 1$. A limited exploration of the 13 Gyr, $\Omega_{tot} < 1$, $\Omega_{vac} = 0$, space with tilt has also been made using $\mathcal{C}_\ell' s$ from Bond and Souradeep (1996).

Fig. 2 illustrates how primary $\mathcal{C}_\ell$'s vary with some of these cosmic parameters. They are normalized to the 4-year dmr(53+90+31)(A+B) data [6, 1, 5]. A "standard" CDM model, with n_s=1, Ω_{tot}=1, H_0=50, Ω_B=0.05, and a 13 Gyr age (hereafter sCDM), is the upper solid curve. Our DMR analysis gives $\sigma_8 = 1.20 \pm 0.08$, far from the $\sigma_8 \sim 0.6\Omega_{nr}^{-0.56}$ target value derived from cluster abundance observations (§ 2.3). (Here $\Omega_{nr} = \Omega_{cdm} + \Omega_{hdm} + \Omega_B$.) An (almost indistinguishable) dotted curve has the same parameters except that it includes a light neutrino with $\Omega_{m\nu} = 0.2$ (and $\Omega_{cdm} = 0.75$). It has $\sigma_8 = 0.83 \pm 0.06$, closer to the cluster value, but a little tilt would help. The upper dashed curve is a vacuum-dominated model with H_0=75 and the 13 Gyr age (and $\Omega_\Lambda = 0.73$, $\Omega_B = 0.02$, $\Omega_{cdm} = 0.24$). It has $\sigma_8 = 1.03 \pm 0.07$, which is OK for cluster abundances. An open CDM model has the $\mathcal{C}_\ell$ peak shifted to higher ℓ; the one shown has $H_0 = 60$ and the 13 Gyr age, with Ω_{tot}=0.33, Ω_{cdm}=0.30, $\Omega_B = 0.035$, and $\sigma_8 \sim 0.5$ (hence too few clusters). By $H_0 = 70$, Ω_{tot} is down to 0.055 at this age. The lower solid curve is a CDM model with reionization at $z_{reh} = 30$, and almost degenerate with it is a tilted CDM model (n_s=0.95 but otherwise standard). Even the nearly degenerate hot/cold and CDM models shown should be distinguishable by COBRAS/SAMBA (e.g., Fig. 5).

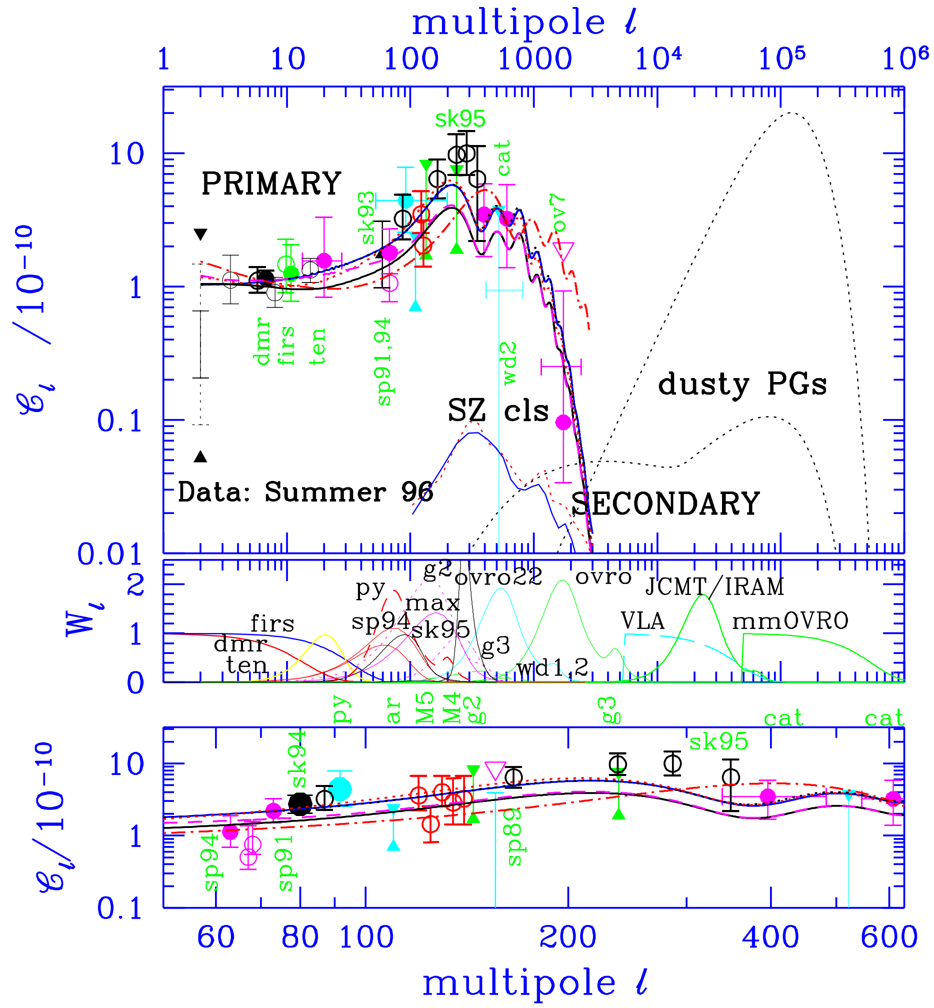

Figure 2: Sample primary and secondary power spectra are compared with the band-power estimates derived for the anisotropy data up to summer 1996. Here $\mathcal{C}_\ell \equiv \ell(\ell+1)\langle|(\Delta T/T)_{\ell m}|^2\rangle/(2\pi)$. The lower panel is a closeup of the first two 'Doppler peaks'. Average filter functions for a variety of experiments are shown in the middle panel. The upper solid primary $\mathcal{C}_\ell$ curve is a COBE-normalized untilted sCDM model, and variants are shown with the same cosmological age and $\Omega_B h^2$, but nonzero tilt, Ω_{hdm} (i.e., $m_\nu > 0$), Ω_{vac} (i.e., $\Lambda > 0$), average curvature (i.e., $\Omega_{tot} < 1$) or weak reionization. They all broadly agree with the data. By contrast, the thermal SZ anisotropy power is way down, the kinematic SZ power is off-scale, and dusty emission power from early galaxies is concentrated at higher ℓ and higher frequency.

1.5 Cosmological Transport

Cosmological radiative transfer is on a firm theoretical footing. Together with a gravity theory (invariably Einstein's general relativity, but the CMB will eventually be used as a test of the gravity theory) and the transport theory for the other fields and particles present (baryons, hot, warm and cold dark matter, coherent fields, i.e., "dynamical" cosmological "constants", *etc.*), we propagate initial fluctuations from the early universe through photon decoupling into the (very) weakly nonlinear phase, and predict *primary anisotropies*, those calculated using either linear perturbation theory (e.g., for inflation-generated fluctuations), or, in the case of defects, linear response theory. The sources driving their development are listed in Table 1.5.

PHYSICAL PROCESSES FOR ANISOTROPY	
PRIMARY SCALAR ANISOTROPIES	
$\Phi/3$	"Naive" Sachs-Wolfe effect: Gravitational Potential
$\frac{1}{4}\frac{\delta\rho_\gamma}{\rho_\gamma}$	photon bunching (acoustic): $\frac{1}{3}\frac{\delta\rho_B}{\rho_B}$ effect, isocurvature effect
$\sigma_T \bar{n}_e \mathbf{v}_e \cdot \hat{q}$	Linear-order Thompson scattering (Doppler)
$2\int_{l.o.s.} \dot{\Phi}$	Integrated Sachs-Wolfe effect
	subdominant anisotropic stress and polarization terms
PRIMARY TENSOR ANISOTROPIES	
$\frac{1}{2}\dot{h}_{+,\times}$	gravity waves (two polarizations)
	subdominant polarization terms
SECONDARY ANISOTROPIES	
ε_{AB}	Linear Weak Lensing: 2D shear tensor
$2\int_{l.o.s.} \dot{\Phi}_{NL}$	Rees-Sciama effect: Response to Φ of nonlinear structure
$\sigma_T \delta n_e \mathbf{v}_e \cdot \hat{q}$	Nonlinear Thompson scattering:
......	Quadratic-order (Vishniac) effect,
......	"kinematic" SZ effect (moving cluster/galaxy)
$\int_{l.o.s.} \psi_K(x)\delta(n_e T_e)$	thermal SZ effect: Compton cooling ($x = E_\gamma/T_\gamma$)
$\int_{l.o.s.} \psi_{dust}(x_d)\rho_d$	(pre/proto)galactic dust emission, ($x_d = E_\gamma/T_d$)
FOREGROUNDS	
	extragalactic radio sources: falling, flat, rising
	IRAS sources and extrapolations to moderate z
	Galactic bremsstrahlung, synchrotron
	Galactic Dust: regular, cool, strange??

Spurred on by the promise of percent-level precision in cosmic parameters from CMB satellites (§ 2.5), a considerable fraction of the CMB theoretical community with Boltzmann transport codes compared their approaches and validated the results to ensure percent-level accuracy up to $\ell \sim 3000$ (COMBA [11]). The arena shifted from figures like Fig. 2 to $\Delta\mathcal{C}_\ell/\mathcal{C}_\ell$ figures with tiny vertical range such as Fig. 5. We look forward to the happy day when these relative difference figures will be used to reveal the remaining tiny residuals in the best fit theoretical model. An important goal for COMBA was speed, since the parameter space we wish to constrain has many dimensions. Most groups have solved cosmological radiative transport by evolving a hierarchy of coupled moment equations, one for each ℓ. Although the equations and techniques were in place prior to the COBE discovery for scalar modes, and shortly after for tensor modes, to get the high accuracy with speed has been somewhat of a challenge. There are alternatives to the moment hierarchy for the transport of photons and neutrinos. In particular the entire problem of photon transport reduces to integral equations in which the multipoles with $\ell > 2$ are expressed as history-integrals of metric variables, photon-bunching, Doppler and polarization sources, as in Table 1.5. The fastest COMBA-validated code uses this method [12].

1.6 Secondary Anisotropies

Secondary anisotropies, with sources listed in Table 1.5, arise from nonlinear structures. They are a nuisance foreground to be subtracted to get at the *primary* primary ones, but also invaluable probes of shorter-distance aspects of structure formation theories, full of important cosmological information. The effect of lensing is to smooth slightly the Doppler peaks and troughs of Fig. 2. $\mathcal{C}_\ell$'s from quadratic nonlinearities in the gas at high redshift are concentrated at high ℓ, but for most viable models are expected to be a small contaminant. Thomson scattering from gas in moving clusters also has a small effect on $\mathcal{C}_\ell$, although it will be measurable in individual clusters. Power spectra for the thermal SZ effect from clusters are larger [13]; examples in Fig. 2 are for a cluster-normalized σ_8=0.7 hot/cold hybrid model (solid, Ω_{hdm}=0.3, h=0.5, $\bar{y} \sim 0.3 \times 10^{-6}(\Omega_{Beff}/0.05)$) and an n_s=0.8 tilted CDM model ($\bar{y} \sim 0.5 \times 10^{-6}(\Omega_{Beff}/0.05)$, with a similar value for n_s=1). Although $\mathcal{C}_\ell^{(SZ)}$ may be small, because the power for such non-Gaussian sources is concentrated in hot or cold spots the signal is detectable, and has been for more than a dozen clusters now at the 5–10 sigma level. $\mathcal{C}_\ell$ for a typical dusty primeval galaxy model is also shown, the larger (arbitrarily normalized) part a shot-noise effect for galaxies with dust distributed over 10 kpc, the smaller a contribution associated with clustering. These anisotropies are very likely to be observable with new instrumentation on submm telescopes (e.g., SCUBA on the James Clerk Maxwell Telescope on Mauna Kea). Similar shot-noise spectra are expected for other extragalactic point sources, e.g., radio galaxies.

2 CMB Parameter Estimation, Current and Future

2.1 The Theorists' Phenomenology of CMB Experiments

We have progressed from the tens of pixels of early $\Delta T/T$ experiments through the thousands for DMR and SK95, conducted by the Princeton group near Saskatoon, Saskatchewan [9]. We will soon be dealing with tens of thousands for long duration balloon experiments and eventually millions for the MAP [16] and COBRAS/SAMBA [17] satellites. How best to analyze statistically these data sets is a subject being developed largely by CMB theorists. Theorists have also taken on an increasingly phenomenological role in LSS studies and many of the same techniques are being applied to both $\Delta T/T$ and LSS data sets. This is opening up into a major subfield. Finding nearly optimal strategies for data projection, compression and analysis which will allow us to disentangle the primary anisotropies from the Galactic and extragalactic foregrounds and from the secondary anisotropies induced by nonlinear effects will be the key to realizing the theoretically-possible precision on cosmic parameters and so to determine the winners and losers in theory space. Particularly powerful is to combine results from different CMB experiments and combine these with LSS and other observations. Almost as important as the end-product is the application of the same techniques to probing the self-consistency and cross-consistency of experimental results.

A phenomenology using few-parameter local models of $\mathcal{C}_\ell$ is often used to probe the experiments. The simplest example has a broad-band power $\langle \mathcal{C}_\ell \rangle_W$

and a broad-band tilt $\nu_{\Delta T}$ over a filter W_ℓ:

$$\mathcal{C}_\ell \;=\; \langle \mathcal{C}_\ell \rangle_W \frac{\mathcal{U}_\ell \, \mathcal{I}[W_\ell]}{\mathcal{I}[W_\ell \mathcal{U}_\ell]} \, , \quad \mathcal{U}_\ell \equiv \frac{\Gamma(\ell + \frac{\nu_{\Delta T}}{2})\Gamma(\ell+2)}{\Gamma(\ell)\Gamma(\ell+2-\frac{\nu_{\Delta T}}{2})} \approx (\ell + \tfrac{1}{2})^{\nu_{\Delta T}} \, . \quad (1)$$

The power law approximation to the Γ–Γ form is excellent for $\ell > 2$. For the (now historical) single and double difference experiments, such as SP89,91,94, MSAM, MAX, Tenerife, one filter, $\overline{W}_\ell$, covering the full ℓ-space probed by the experiment gives most of the useful information. This is the nature of most of the filters of Fig. 2. If it is found that an experiment can distinguish various $\nu_{\Delta T}$, then it is useful to break the ℓ-range probed by the average filter into a number of sub-bands: e.g., DMR and SK95 have enough data to warrant breaking the ℓ-range probed into a few filters, and new experiments under construction (long duration balloons, interferometers, MAP, COBRAS/SAMBA) will require many filters.

The COBE DMR data has been the most intensely analyzed set so far, with many statistical methods developed and applied to it (often by theorists), involving linear, quadratic and some nonlinear statistics, using Bayesian (likelihood) and frequentist (Monte Carlo) methods. When models obeying eq.(1) over the DMR ℓ-band are explored in the range $0 \leq \nu_{\Delta T} \leq 3$, after marginalization over the bandpower $\langle \mathcal{C}_\ell \rangle_{\overline{W}_{dmr}}$, using Bayesian methods, we find $1 + \nu_{\Delta T} = 1.07^{+.27;.52}_{-.29;.58}$ for 53+90+31 GHz. First errors are 1σ, second are 2σ. There is good agreement among many statistical methods on this index [6]. Other frequency combinations give compatible results within the errors: $0.97^{+.30;.57}_{-.32;.64}$ for 53+90 GHz; $1.15^{+.31;.59}_{-.33;.66}$ for 53 GHz; $1.27^{+.40;.77}_{-.43;.86}$ for 90 GHz. For the 31 GHz map, there is a residual bremsstrahlung contribution that lowers the index to 0.3, with large errors.

The bandpowers as a function of $\nu_{\Delta T}$ for the various frequency channels are also in good agreement: $\langle \mathcal{C}_\ell \rangle^{1/2}_{dmr} \approx [0.82 + 0.26(1 - \frac{\nu_{\Delta T}}{2})^{2.8}] \times 1^{+.07}_{-.06}$ for the 53+90+31 GHz is reasonably insensitive to modest variations in $\nu_{\Delta T}$. The form holds for all individual frequency channels, except 0.82,0.26 change: (0.88,0.24 for 53 GHz, 0.95,0.15 for 90 GHz, 0.90,0.08 for 31 GHz). The 7% amplitude error bar also grows: 8% for 53 GHz, 11% for 90 GHz, 16% for 31 GHz [1].

A byproduct of the signal-to-noise eigenmode method [14, 1] used in this analysis are Wiener-filtered maps of Fig. 2.1 which give the statistically-averaged signal given the data and a best-fit signal model. These optimally-filtered maps are insensitive to variations in the model theory. The robustness of features in the maps and the weak frequency dependence in the bandpowers are strong arguments that what is observed is on the sky with a primary anisotropy origin, made stronger by the compatible amplitudes and positive cross-correlations with the FIRS and Tenerife data sets.

Fig. 2 shows that though a power law fit is reasonable for the COBE data, it is poor over the ~ 50 to ~ 400 ℓ-range SK95 probes. A shape which roughly fits the rise in the power is more appropriate, e.g., the scalar-only sCDM sequence with variable n_s. It has been usual in the COBE literature to denote $1+\nu_{\Delta T}$ by n, inviting confusion with the index for the primordial adiabatic fluctuation power spectrum, n_s. For CDM models with Ω=1 and Ω_{vac}=0, there is a rough relation over the DMR band: $\nu_{\Delta T} \approx 0.15+\nu_s$, where $\nu_s = n_s - 1$. If σ_8 is marginalized for a sequence of models with $0.5 < n_s < 1.5$, the result for the primordial index is $n_s = 1.02^{+.23;.41}_{-.25;.52}$ for scalar perturbations only (no gravity waves, ν_t=0) and $1.02^{+.23;.40}_{-.18;.46}$ (with gravity waves and ν_t=ν_s), rather encouraging for the nearly scale invariant models preferred by inflation theory. (σ_8 has a stronger dependence upon n_s than the bandpower does.)

The CDM tilt sequence provides a moderately good fit to the SK95 data as long as n_s is allowed to exceed unity: e.g., the 13 Gyr $H_0 = 50$ sCDM sequence gives [5] $n_s = 1.37^{+.13;.13}_{-.30;.62}$, with similar error bars to DMR (upper range saturating at the upper limit imposed on n_s). The results do not change much as we change Ω_B, Ω_{vac}, the age of the Universe. The better fitting open 13 Gyr model with $H_0 = 55$, Ω=0.60 has the interesting value $n_s = 0.96^{+.30;.54}_{-.31;.46}$, but no determination at 2σ.

2.2 Parameters from the CMB, Current State

Combining CMB anisotropy experiments probing different ranges in ℓ-space improves parameter estimates because of the much improved baseline. Current band-powers, shown in Fig. 2 and 4, broadly follow inflation-based expectations, but may still include residual signals. Jaffe and I [5] have undertaken full Bayesian statistical analysis of the 4 year DMR, SP94 and SK94/SK95 data sets, taking into account all correlations among pixels in the data and theory. This contrasts with the seductive but flawed approach of using all the bandpowers and their error bars in Fig. 2 as independent points with Gaussian errors.

With current errors on the data, simultaneously exploring the entire parameter space is not useful, so we restricted our attention to various sub-

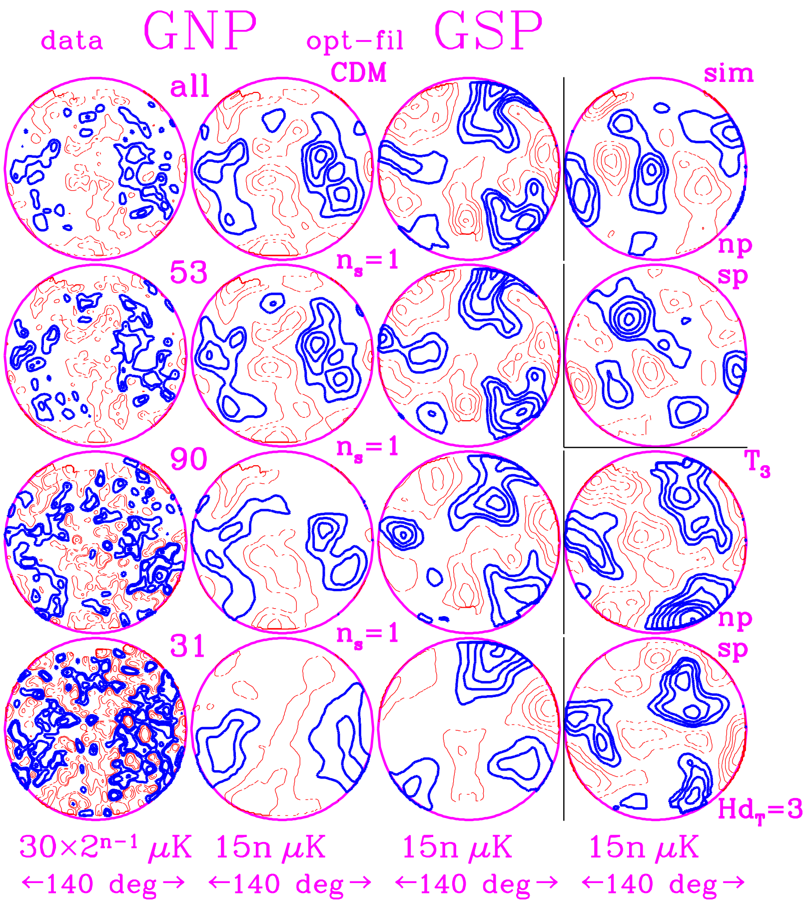

Figure 3: The first column shows unfiltered 140° diameter *dmr* A+B maps centered on the North Galactic Pole, the second shows them after Wiener-filtering (with monopole, dipole and quadrupole removed), the third the South Pole version, with the *nth* contour as noted and negative contours heavier than positive ones. The maps all use n_s=1 CDM models (HCDM looks the same) with σ_8 chosen to match the DMR data and have been smoothed by a 1.7° Gaussian filter. *all* is 53+90+31A+B. Although higher noise results in filtering on greater angular scales, the large scale features of all maps are the same. This is also borne out by detailed statistical comparisons map to map. The last column shows some theoretical realizations, after optimal filtering. The first two rows are the NGP and SGP for a n_s=1 CDM model. The lower two rows are for a flat ($\nu_{\Delta T}$=0) model with a 3-torus topology, with repetition length d_T = 9000 h^{-1} Mpc in all three directions, a model strongly ruled out because of the high degree of positive correlation between the North and Southern hemispheres that the periodicity induces.

regions, such as $\{\sigma_8, n_s, \mathrm{h} \,|\, \mathrm{fixed}\, t_0, \Omega_B \mathrm{h}^2\}$, because of the length of time required for a complete statistical treatment of each data set per model $\mathcal{C}_\ell$. Even so, we made use of signal-to-noise compression of the data (by factors of 3) in order to make the calculations of the likelihood tractable (without loss of information or accuracy). Otherwise what took a week of computer time to form the likelihood functions $\mathcal{L}(\sigma_8, n_s, \mathrm{h} \,|\, \mathrm{fixed}\, t_0, \Omega_B \mathrm{h}^2)$ would have taken a year.

The n_s constraints are quite good, but H_0 for fixed age is not that well determined by the CMB data alone. The 15 Gyr sequence with $\Omega_B \mathrm{h}^2$ fixed at 0.0125 fits better than the 13 Gyr sequence, which in turn fits better than the 11 Gyr sequence for $n_s \leq 1$. If we consider just the 13 Gyr sequence with variable Ω_B for $n_s = 1$, $\Omega_B = 0.17^{+.03}_{-.08}$ is preferred, but if we allow n_s to exceed one then a low Ω_B is preferred (and $n_s = 1.15$).

2.3 Parameters from the CMB+LSS, Current State

We have always combined CMB and LSS data in our quest for viable models. Fig. 1 shows how the two are connected. As we have seen, the DMR data precisely determines σ_8 for each model considered. For the COBE-normalized density power spectra to thread the "eye of the needle" associated with cluster abundances severely constrains the parameters determining them (see Fig. 1). Similar constrictions arise from galaxy-galaxy and cluster-cluster clustering observations. Smaller angle CMB data (e.g., SP94, SK95) are consistent with these models [5], and will soon be powerful enough for the CMB by itself to offer strong selection, but this will definitely not diminish the combined LSS-CMB phenomenology.

The shape of the galaxy-galaxy power spectrum inferred from the APM and redshift surveys is compatible with the range $0.15 \lesssim \Gamma + \nu_s/2 \lesssim 0.3$, where $\Gamma \approx \Omega_{nr}\, \mathrm{h}\, [\Omega_{er}/(1.68\Omega_\gamma)]^{-1/2}\, e^{-(\Omega_B(1+\Omega_{nr}^{-1}(2\mathrm{h})^{1/2})-0.06)}$ is the shape parameter. The sCDM shape has $\Gamma \approx 0.5$. To get $\Gamma + \nu_s/2$ in the observed range one can: lower h, lower Ω_{nr} (ΛCDM, OCDM), raise Ω_{er}, the density parameter in relativistic particles ($1.68\Omega_\gamma$ with 3 species of massless neutrinos and the photons), e.g., as in τCDM, with a decaying ν of lifetime τ_d and $\Gamma \approx 1.08\Omega_{nr}\mathrm{h}(1 + 0.96(m_\nu \tau_d/\mathrm{keV\ yr})^{2/3})^{-1/2}$; raise Ω_B; tilt $\nu_s < 0$ (TCDM), for standard CDM parameters, e.g., $0.3 \lesssim n_s \lesssim 0.7$ would be required. Adding a hot dark matter component gives a power spectrum characterized by more than just Γ.

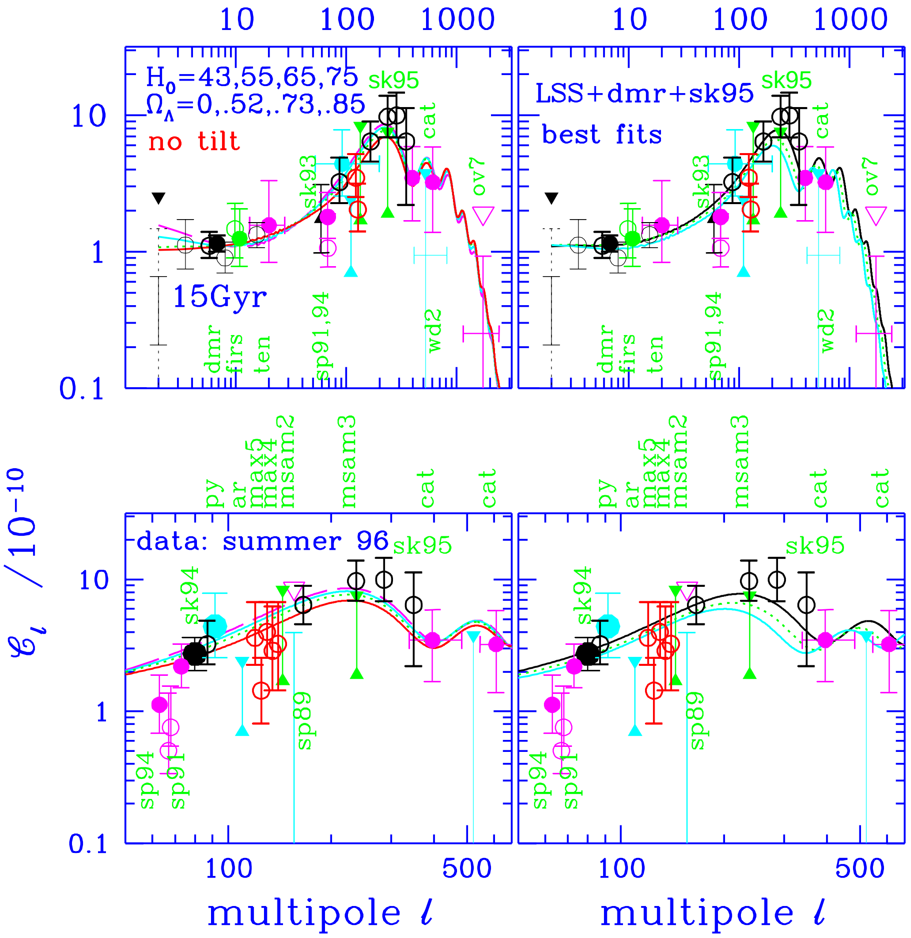

Figure 4: Left is a sample sequence of inflation-motivated models in Bond and Jaffe (1996), here the 15 Gyr sequence, varying H_0 and Ω_{vac}, for n_s=1 (and with Ω_Bh^2=0.0125 fixed). It is clearly not feasible to get a good value of Ω_{vac} from the data, as is borne out by the statistics. n_s is also allowed to vary in the sequence, gives more dramatic changes so good constraints are placed on n_s: $1.05^{+.12}_{-.08}$ with gravity waves. 13 Gyr ($1.11^{+.11}_{-.10}$) and 11 Gyr sequences were also treated. Similar n_s limits are obtained when the LSS data is added, and then the data prefers a nonzero Ω_{vac}. Right shows best-fit models for the 11,13,15 Gyr sequence with n_s and Ω_{vac} varying, for $\Omega_B\mathrm{h}^2$ = 0.0125, using DMR+SP94+SK95 plus cluster abundances and large scale flow estimates of σ_8 and the APM galaxy clustering estimate of the power spectrum shape plus tilt parameter. These are: 15 Gyr, H_0=55, Ω_{vac}=0.52, σ_8 = 0.97, n_s=1.0; 13 Gyr, H_0=65, Ω_{vac}=0.56, σ_8 = 1.17, n_s=1.0 is 1σ down; 11 Gyr, H_0=85, Ω_{vac}=0.69, σ_8 = 1.49, n_s=1.05 is 2σ down.

The approach we used in [5] to add this information to the CMB likelihood functions was to design prior probabilities for $\Gamma+\nu_s/2$ and $\sigma_8\Omega_{nr}^{0.56}$, reflecting the current observations, but with flexible and generous non-Gaussian and asymmetric forms to ensure the priors can encompass possible systematic problems in the data. For example, our choice for $\sigma_8\Omega_{nr}^{0.56}$ was quite flat over the 0.55 to 0.70 range, but fell off by 0.50, although some authors actually prefer this value.

Some best fit models when these LSS priors are included are listed in Fig. 4. Sample parameter estimations are model dependent. For example, using only the 4-year *dmr* data and these priors we get $n_s = 0.76^{+.03;.06}_{-.03;.06}$ with gravity waves, $n_s = 0.61^{+.04;.09}_{-.04;.08}$ without for $H_0 = 50$ sCDM, with values slightly increased when SK95 and SP94 are added. (With $\Omega_{m\nu} = 0.2$ of the dark matter in massive neutrinos, we get $n_s = 0.99^{+.03;.06}_{-.03;.06}$ with GW, $n_s = 0.97^{+.04;.08}_{-.05;.10}$ without.) For $H_0 = 70$ and $\Omega_{vac} = 0.66$, we get $n_s = 0.99^{+.03;.06}_{-.02;.04}$. The preferred Hubble parameter for the $n_s = 1$ sequence is 67 ± 3 ($\Omega_{vac} \approx 0.60$).

When H_0 (range 50 to 100 for the 13 Gyr sequence) is marginalized, the LSS+DMR+SK95+SP94 data gives $1.07^{+.13;.24}_{-.08;.12}$ with GW and a similar number without GW. When all n_s are marginalized, we obtain $H_0 = 70 \pm 4$ ($\Omega_{vac} \approx 0.66$) with GW, 63 ± 5 ($\Omega_{vac} \approx 0.50$) without. Similarly the 13 Gyr open sequence also prefers a $\Omega_{tot} < 1$, but $H_0 \sim 55$. For the 15 Gyr CDM sequence, the result for n_s after marginalization over all $H_0 \geq 43$ (the value for the $\Omega_{vac} = 0$ model) is $1.03^{+.14;.23}_{-.04;.08}$ with GW, $1.06^{+.11;.20}_{-.09;.16}$ without; and when n_s is marginalized, $H_0 = 55 \pm 4$ ($\Omega_{vac} \approx 0.5$) with GW, 49 ± 5 ($\Omega_{vac} \approx 0.3$) without.

Should these small error bars be taken seriously? They are driven by just the DMR plus LSS results. I would be rather surprised if σ_8 from cluster abundances is drastically revised; and as we have seen, the DMR results are quite robust. The reason the errors are small is typically that the CMB data has a likelihood peaked at high $\sigma_8 \gtrsim 1$, while the LSS one peaks at 0.6 or so, so the product is narrow, but with a small likelihood. This asymmetry is not as pronounced for HCDM models with a light massive neutrino, and the model does not require $\Omega_{vac} > 0$, but it does help a bit.

2.4 CMB Constraints on Ultra-large Scale Structure

The "beyond our horizon" land in Fig. 1 is actually partly accessible because long waves contribute gentle gradients to our observables. Constraints on such "global parameters" as average curvature are an example, $d_c > 1.1 H_0^{-1}$, though not yet very restrictive. One may also probe whether a huge bump or deficit in power exists just beyond $k^{-1} \sim H_0^{-1}$, but this has not been much explored. The remarkable non-Gaussian structure predicted by stochastic inflation theory would likely be too far beyond our horizon for its influence to be felt. The bubble boundary in hyperbolic inflation models may be closer and its influence shortly after tunneling occurred could possibly have observable consequences for the CMB. Theorists have also constrained the scale of topology in simple models (Fig. 2.1). We [15] find the torus scale is $d_T/2 > 1.1(2H_0^{-1}) = 6600\,\mathrm{h}^{-1}$ Mpc from DMR for flat equal-sided 3-tori at the 95% confidence limit, slightly better than other groups find since we used full map statistics. The constraint is not as strong if the repetition directions are asymmetric, $> 1.5 H_0^{-1}$ for 1-tori from DMR. It is also not as strong if more general topologies are considered, e.g., the large class of compact hyperbolic topologies.

2.5 Parameters from the CMB, Future

Quite an industry has developed showing how well future long duration balloon flights, LDBs, (ACE, Boomerang, Maxima, Top Hat,...), interferometers (VSA, CBI, VCA) and especially the satellites MAP and COBRAS/SAMBA could do in measuring the radiation power spectrum and cosmological parameters if foreground contamination is ignored [18, 19, 20, 17, 22, 21], and that is what is done here in Table 1, following our work in [21]. Particular note should be made of the estimates made by [20] and [17]: these were quite influential in making the case for MAP and COBRAS/SAMBA funding. Fig. 5 gives a closeup view of how very fine differences in the theoretical $\mathcal{C}_\ell$'s can be measured using detector sensitivities and the long observing times appropriate for satellite experiments roughly suitable for MAP [16] and the higher resolution COBRAS/SAMBA [17].

Consider a class of cosmological models with Gaussian-distributed temperature anisotropies defined by a parameter set $\{y_A\}$. For definiteness here we shall use the parameter space $\{\langle \mathcal{C}_\ell \rangle_B, n_s, r_{ts}, \Omega_B \mathrm{h}^2, \mathrm{h}, \Omega_{vac}, \Omega_{tot}, \Omega_{m\nu} \mathrm{h}^2, \zeta_C\}$,

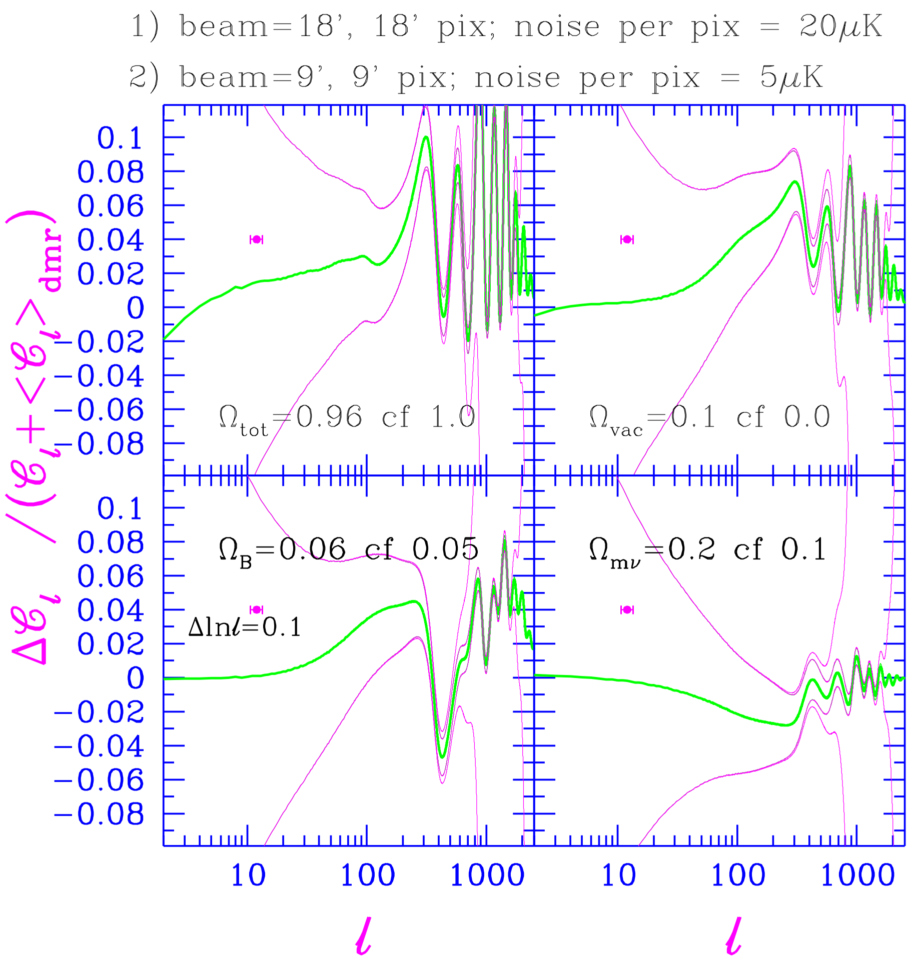

Figure 5: This shows the ability of satellites to measure cosmic parameters to high accuracy. The relative difference of the power spectrum in question from a comparison spectrum (both normalized to the 4-year *dmr* (53+90+31)A+B COBE maps) are shown so that the few percent deviations can be clearly seen over the entire ℓ range. The lighter lines are $1 - sigma$ error bars for all-sky coverage (averaged over the smoothing width shown, with $\frac{1}{2}\Delta\ln\ell = 0.05$) and include cosmic variance (dominant at low ℓ) and pixel noise at 20μK or 5μK (dominant at high ℓ), with the very rapid growth relative to the theory curve at high ℓ coming from the finite beam-size (with the *fwhm* indicated, corresponding to a Gaussian filters in multipole space of $\ell_s = 450$ and 900 respectively). The first choice is motivated by NASA's MAP parameters, the second by ESA's COBRAS/SAMBA parameters, if the entire sky were usable (errors scaling $\propto f_{sky}^{-1/2}$). The models shown are mostly variants of the sCDM model.

with the residual energy density, $\Omega_{tot}-\Omega_{vac}-\Omega_B$, assumed to be in cold dark matter. $\langle \mathcal{C}_\ell \rangle_B$ is the total bandpower for the experiment (or the one with the largest ℓ-coverage if a number of experiments are considered) and ζ_C the Compton optical depth from a reheating redshift z_{reh} to the present. The ratio of tensor to scalar quadrupole powers, $r_{ts} \equiv \mathcal{C}_2^{(T)}/\mathcal{C}_2^{(S)}$, is a sensitive function of ν_t, but also depends on $\nu_s - \nu_t$, Ω_{vac}, etc. [1]. However, for nearly scale invariant models, $\delta r_{ts} \propto \delta \nu_t$, so it is reasonable to vary only one of them; here r_{ts} is chosen.

To estimate the errors, we need to evaluate the likelihood function $\mathcal{L}(\{y_A\})$. To make this simple, we assume the noise is uniform over a regular connected patch covering a fraction f_{sky} of the sky, although we allow for variations in the noise in different frequency channels; i.e., the data correlation matrix between frequency channels c and spatial pixels p, $C_{Dcp,c'p'}$, is of form $C_{Dc,c'}\delta_{pp'}$. Assume it is diagonal. The noise per pixel of length ϖ_{pix} in channel c is $\sigma_{c,pix} = C_{Dc,c}^{1/2}$, and the pixel noise of the summed map (the linear combination sensitive to primary CMB anisotropies) is $\overline{\sigma}_{pix} \equiv \left[\sum_c \sigma_{c,pix}^{-2}\right]^{-1/2}$. The power spectrum of the noise is therefore white, $\overline{\mathrm{C}}_{D\ell} = \overline{\sigma}_{pix}^2 \varpi_{pix}^2$, a combination invariant under change of pixel size for fixed experimental parameters. The theoretical signals are also diagonal in the ℓm basis (or angular wavenumber basis for a rectangular patch), with power spectra of form $\mathrm{C}_{T\ell}\mathcal{B}_{c\ell}\mathcal{B}_{c'\ell}$, where $\mathcal{B}_{c\ell}$ is the filter function associated with the beam for channel c. Its noise-weighted average, $\overline{\mathcal{B}}_\ell$, is defined by $\overline{\mathcal{B}}_\ell^2 \equiv \left[\sum_c \mathcal{B}_{c\ell}^2 \sigma_{c,pix}^{-2}\right] / \left[\sum_c \sigma_{c,pix}^{-2}\right]$.

We also assume the deviations in the parameters about the maximum likelihood values $\{y_{Am}\}$ are sufficiently small that we can approximate $\mathcal{C}_\ell(\{y_A\})$ by a linear variation. Choose the parameter set $\{y_{Am}\}$ which approximately maximizes the likelihood (e.g., using quadratic estimators to determine the power spectrum from the data and fitting it with $\mathcal{C}_\ell(y_{Am})$). Expand $\ln \mathcal{L}$ to quadratic order in $\delta y_A \equiv y_A - y_{Am}$. Adjust the y_{Am} so that the linear term $\partial \ln \mathcal{L}/\partial y_A$ vanishes, thereby yielding a Gaussian approximation with zero mean to the likelihood,

$$\mathcal{L} \sim \mathcal{L}_m \exp[-\tfrac{1}{2}\sum_{AB} \overline{S}_{AB}\delta y_A \delta y_B]\, , \quad \overline{S}_{AB} = \sum_\ell \frac{\partial \mathcal{C}_{T\ell}}{\partial y_A} (\Delta \mathcal{C}_{T\ell})^{-2} \frac{\partial \mathcal{C}_{T\ell}}{\partial y_B}\, , \quad (2)$$

$$\Delta \mathcal{C}_{T\ell} \approx \frac{\sqrt{2}}{\sqrt{(2\ell+1)f_{sky}}} (\mathcal{C}_{T\ell} + \overline{\mathcal{C}}_{D\ell}\overline{\mathcal{B}}_\ell^{-2})\, , \, , \quad \overline{\mathcal{C}}_{D\ell} \equiv \frac{\ell(\ell+1)\overline{\mathrm{C}}_{D\ell}}{2\pi}\, .$$

Here the parameter derivatives $\partial \mathcal{C}_{T\ell}/\partial y_A$ are evaluated at y_{Am}, as is the $\mathcal{C}_{T\ell}$ in the variance $(\Delta \mathcal{C}_{T\ell})$ given by eq.(3). In practice, the $\partial \mathcal{C}_{T\ell}/\partial y_A$ are determined through finite differences, with variation Δy_A roughly covering the error bar range. To accurately compute this Fisher matrix, $\overline{S}_{AB}$, the precision of the COMBA-validated [11] $\mathcal{C}_\ell$'s is needed [21].

The form for $\overline{S}_{AB}$ applies to multichannel configurations provided the channel-weighted quantities $\overline{\mathrm{C}}_{D\ell}$ and $\overline{\mathcal{B}}_\ell^2$ are used. The Fisher matrices for independent experiments just add. $\overline{\mathcal{B}}_\ell$ has been divided out to show that the effective noise level in $\mathcal{C}_\ell$ determination picks up enormously above $\ell_s \sim (0.425\theta_{fwhm})^{-1}$. An appropriately smoothed (binned) version of $\Delta \mathcal{C}_{T\ell}/\mathcal{C}_{T\ell}$ is what is plotted in Fig. 5. The sum over ℓ is naturally cut off well above ℓ_s. It should also have a lower cutoff ℓ_{cut} reflecting the finite size of the regions mapped, e.g., the fundamental mode, $\ell_{cut} = 2\pi/\varpi_{box}$, for a rectangular patch of width ϖ_{box}. For given detector specification, $\overline{\mathrm{C}}_{D\ell}$ scales as f_{sky}/t_{obs}. Whether the observing time t_{obs} should be spent doing large patches at the expense of increased noise or small at the expense of enhanced cosmic variance is usually defined by experimental limitations and issues of foreground control.

Using Bayes' theorem, we can write the probability of the theoretical parameters, given the observations and the class of theories being tested, $P(\{y_A\}|\mathrm{OBS, TH}) \propto \mathcal{L}(\{y_A\})P(\{y_A\}|\mathrm{prior})$, where the assumed prior probability distribution $P(\{y_A\}|\mathrm{prior})$ can reflect *a priori* maximal ignorance, or take into account constraints from other information such as large scale structure observations, as in § 2.3. The proportionality constant is related to the probability that the class of theories is correct given the observations. We choose a Gaussian *prior* probability for the fluctuations $y_A - y_{A0}$, with covariance matrix H_{AB}, $P(\{y_A\}|\mathrm{prior}) = \exp[-\frac{1}{2}(y-y_0)^\dagger H^{-1}(y-y_0)]$. The limit of very large eigenvalues of H corresponds to no prior information on the δy_A. The prior information will presumably have a different maximum set of parameters, $\{y_{A0}\}$, than the $\{y_{Am}\}$ of $\mathcal{L}$, resulting in an adjustment for the maximum of $P(\{y_A\}|\mathrm{OBS, TH})$, $\tilde{\mathbf{y}}_m = \mathbf{y}_m + (1+HS)^{-1}(\mathbf{y}_0 - \mathbf{y}_m)$, an overall probablity diminished to the degree that $\mathbf{y}_0$ and $\mathbf{y}_m$ are mismatched (e.g., what happened when the sCDM $\mathcal{L}$ was combined with the LSS prior in § 2.3), and a probability for the parameter fluctuation $\delta y_A \equiv y_A - \tilde{y}_{Am}$ with mean zero and variance $(\overline{S} + H^{-1})^{-1}$.

If we are interested in the error bars on δy_A irrespective of the values of the other variables, we would marginalize over these. The 1-sigma error is then $\pm\sqrt{(\overline{S}+H^{-1})^{-1}_{AA}}$, the numbers quoted in the Table 1. The columns designated *np* in Table 1 have no prior constraints on the parameter fluctuations, i.e., the eigenvalues of H are very large; otherwise the matrix H is assumed to be diagonal with widths 1 on $\langle \mathcal{C}_\ell \rangle^{1/2}$, 0.5 on n_s, 5 on r_{ts}, 0.3 on $\Omega_B \mathrm{h}^2$, 0.5 on H_0, 1 on Ω_{vac}, 3 on ζ_C, 1 on Ω_{tot}, 0.3 on $\Omega_{m\nu}(2\mathrm{h})^2$.

Generally the errors in the parameters will be correlated through non-diagonal components of $(\overline{S}+H^{-1})^{-1}$. There are linear combinations of the parameters which are uncorrelated, namely $(\overline{S}+H^{-1})^{1/2}\delta y$. When the eigenvalues of $(\overline{S}+H^{-1})$ are rank ordered, from high to low, the variable combinations corresponding to the top ones will be very accurately determined, while those for the lowest may be very poorly determined, representing the degenerate directions in parameter space. Such parameter eigenmode combinations are therefore a natural generalization of the crude degeneracy parameter $\tilde{n}_s$ introduced in [23].

In Table 1, we assumed the correct underlying theory is an untilted sCDM one. The first two columns use only the 2 parameter tilted sequence with other parameters fixed for the accuracy estimates, but the orthogonal combinations were determined for the 9 parameter case. The Table also applies the method to DMR, using the average noise in the 53+90+31 GHz map for $\overline{\sigma}_{pix}$, $30\mu K$ per 5.2° pixel. The method does predict that the bandpower is obtained to 7%, and n_s to 20% accuracy, as was obtained in § 2.1. The NCP numbers are SK95-like, for a 9° radius patch, and it does indeed show that one can get two combinations of parameters by combining with DMR, the basic result of the limited parameter studies of § 2.2, $\langle \mathcal{C}_\ell \rangle$ or σ_8, and n_s. The third column gives values similar to what one might expect in a bolometer-based LDB experiment (using conservative numbers from the TopHat collaboration that took account of excess noise associated with foreground removal). Proposed HEMT-based LDB experiments, such as UCSB's BEAST using 40 GHz HEMTs, might also achieve similar accuracy (though in this case without the wide frequency coverage to remove foregrounds). Because of the limited sky coverage, there is an effective cutoff in the ℓ that can be well-probed for NCP and LDB, and the numbers improve when one adds DMR to extend the baseline, as in § 2.2 when DMR was added to SK95.

We adopt the current specifications for MAP [16] and COBRAS/SAMBA [17]. These are likely to evolve. Of the 5 HEMT channels for MAP, we assume the 3 highest frequency channels, at 40, 60 and 90 GHz, will be dominated by the primary cosmological signal, and adopt *fwhm* beams shown in the Table. The average noise power is also shown. MAP^{++} assumes a 25% improvement in beams and in HEMT noise and 2 years of observing. For COBRAS/SAMBA, which has both HEMTs and bolometers, we take the 3 best bolometer channels at 150, 217 and 353 GHz to be the primary cosmological ones, with *fwhm* beams 10, 7, 4.4 arcminutes and noise the remarkable 3.4, 3.9 and 14 μK per $10'$ pixel, respectively. We also assumed $f_{sky} = 0.65$ will be usable, the same as the fraction used in the analysis of the 4-year *dmr* data.

These idealized studies do not take into account the cost of separating the many components expected in the data, in particular Galactic and extragalactic foregrounds. The effects of Sunyaev-Zeldovich fluctuations on the power spectrum are not large (see Fig. 2). However the power comes from the clusters and so non-Gaussian aspects of this "foreground" are important. Little is known about high redshift extragalactic sources in the sub-mm. The shape of the power spectrum will have a $\sim \ell^2$ part just from the source counts, and could also have a tail into lower ℓ associated with clustering (as in Fig. 2). By contrast, much is known about the abundance of extragalactic radio sources as a function of flux at long wavelengths. However extrapolations to higher frequencies are required, some poorly known fraction of the sources have flat spectra (in I_ν), and it is not known how much of a problem this will be in the optimal 50-250 GHz observing window for the CMB. The $\sim \ell^2$ Poisson part should strongly dominate.

There is currently some optimism that the Galactic foregrounds may not be a severe problem e.g., [16, 17]. The observed structure of the far-infrared emission, dominated by the dust-laden Cirrus clouds discovered by the IRAS satellite, is rather filamentary with a power spectrum rising towards low ℓ as $\mathcal{C}_\ell \propto \ell^{-1}$. Galactic bremsstrahlung also has a ℓ^{-1} power spectrum, found using the *dmr* data. The amplitude is sufficiently small that these foregrounds should not overly contaminate high precision experiments at $\sim$ 100 GHz. The complication of non-Gaussian concentration of power and the possible multicomponent nature of the dust could compromise this rosy picture.

We can therefore look forward to the day phenomenological theorists will have optimally-analyzed LDBs/VSA/CBI/VCA/MAP/COBRAS/SAMBA and we know the power spectrum and cosmic parameters to wonderful precision. What will it mean? It may not be clear. Take inflation as an example. There

Param	DMR	NCP +DMR	LDB +DMR	MAP np	MAP	MAP^{++} np	COSA np
$\overline{\mathrm{C}}_{D\ell}/10^{-15}$	950	7	1.5	1.5	1.5	.5	.007
f_{sky}	.65	.006	.028	.65	.65	.65	.65
ℓ_s	17	270	400	465	465	620	1850
ℓ_s		17	17	345	345	460	1140
ℓ_s				255	255	340	785
ℓ_{cut}	3	23	12	2	2	2	2
Orthogonal Parameter Combinations within ε							
$\varepsilon < 0.01$	0/9	0/9	1/9	2/9	3/9	3/9	5/9
$\varepsilon < 0.1$	1/9	2/9	4/9	6/9	6/9	7/9	8/9
Single Parameter Errors from Marginalizing Others							
$\langle \mathcal{C}_\ell \rangle^{1/2}$	.07	.03	.021	.017	.017	.014	.009
n_s	.20	.05	.19	.19	.13	.08	.008
r_{ts}	0**F**	0**F**	1.0	1.0	.7	.5	.1
$\Omega_B \mathrm{h}^2$	0**F**	0**F**	.3**P**	.23	.16	.11	.009
H_0	0**F**	0**F**	.18	.13	.09	.05	.007
Ω_{vac}	0**F**	0**F**	.8	.9	.6	.6	.03
ζ_C	0**F**	0**F**	.3	.23	.19	.16	.09
Ω_{tot}	0**F**	0**F**	.13	.13	.09	.06	.006
$\Omega_{m\nu}(2\mathrm{h})^2$	0**F**	0**F**	.24**P**	.10	.10	.06	.02

Table 1: Sample idealized DMR, NCP, LDB, MAP, COBRAS/SAMBA parameter determinations. The best fit to the data was chosen to be the standard CDM model. The results are of course sensitive to which model we choose. **F** means the parameter value was constrained to the sCDM value. **P** means the prior constraint controls that parameter's value. $\langle \mathcal{C}_\ell \rangle^{1/2}$, $\Omega_B \mathrm{h}^2$ and H_0 are relative errors. NCP denotes earth-based observations covering a 9° radius patch, similar to the SK95 observations. The LDB parameters are based upon one week's observing with the bolometer-based TopHat experiment with 65% of a 24° diameter patch being usable. HEMT-based LDBs (e.g., UCSB's BEAST) could in principle achieve similar accuracy levels. MAP^{++} assumes a 25% improvement in beams and in HEMT noise over the originally proposed MAP parameters of columns 5 and 6, and 2 years as opposed to 1 of observing.

will be attempts, undoubtedly optimal ones, to reconstruct the inflaton's potential, but all of our CMB and LSS observations actually access only a very small region of the potential, and even this will be fuzzily determined if we allow too much freedom in parameter space. Still even a fuzzy glimpse is worth the effort. Most fun will be when phenomenology teaches us that non-baroque inflation and defect models fail and howling packs of theorists will hunt the elusive generator following trails well marked by the data.

Acknowledgements: Many of the results in the paper are from active collaborations with George Efstathiou and Max Tegmark, Andrew Jaffe and Lloyd Knox, Dmitry Pogosyan and Tarun Souradeep.

References

[1] Bond, J.R. 1996, *Theory and Observations of the Cosmic Background Radiation*, in "Cosmology and Large Scale Structure", Les Houches Session LX, August 1993, ed. R. Schaeffer, Elsevier Science Press, and references therein.

[2] Peacock, J.A. 1996, preprint

[3] Vogeley, M.S. & Szalay, A.S. 1996, preprint

[4] Fixsen, D.J. et al. 1996, Ap. J., in press.

[5] Bond, J.R. & Jaffe, A. 1996, *Cosmological Parameter Estimation Combining sub-degree CMB experiments with COBE*, in Proceedings of the XXXI Rencontre de Moriond, ed. F. Bouchet, Edition Frontières; CITA preprint

[6] Bennett, C. et al. 1996 Ap. J. Lett., **464**, 1; and 4-year DMR references therein. Hinshaw, G. et al. 1996, Ap. J. Lett., **464**, 17 *dmr*

[7] J.O. Gundersen et al. 1995 Ap. J. Lett., **443**, L57 *sp94*.

[8] Netterfield, C.B., Jarosik, N., Page, L. & Wilkinson, D. 1995, Ap. J. Lett. **455**, L69. *sk94*.

[9] Netterfield, C.B., Devlin, M.J., Jarosik, N., Page, L. & Wollack, E.J. 1996, Ap. J., submitted *sk95*.

[10] Chaboyer, B. et al. 1996, Science, in press.

[11] Bertschinger, E., Bode, P., Bond, J.R., Coulson, D., Crittenden, R., Dodelson, S., Efstathiou, G., Gorski, K., Hu, W., Knox, L., Lithwick, Y., Scott, D., Seljak, U., Stebbins, A., Steinhardt, P., Stompor, R., Souradeep, T., Sugiyama, N., Turok, N., Vittorio, N., White, M., Zaldarriaga, M. 1995, ITP workshop on *Cosmic Radiation Backgrounds and the Formation of Galaxies*, Santa Barbara

[12] Seljak, U. & Zaldarriaga, M. 1996, preprint.

[13] Bond, J.R. & Myers, S. 1996, Ap. J. Supp. **103**, 1.

[14] Bond, J.R. 1994, Phys. Rev. Lett. **74**, 4369.

[15] Bond, J.R., Pogosyan, D., Sokolov, I. & Souradeep, T. 1996, preprint; Bond, J.R., Pogosyan, D. & Souradeep, T. 1996, preprint.

[16] Bennett, C. et al. 1996, MAP experiment home page, http://map.gsfc.nasa.gov

[17] Bersanelli, M. et al. 1996, COBRAS/SAMBA, The Phase A Study for an ESA M3 Mission, preprint; home page, http://astro.estec.esa.nl/SA-general/Projects/Cobras/cobras.html

[18] Knox, L. 1995, Phys. Rev. D **52**, 4307.

[19] Tegmark, M. & Efstathiou, G. 1996, M.N.R.A.S. in press.

[20] Jungman, G., Kamionkowski, M., Kosowsky, A. & Spergel, D.N. 1996, Phys. Rev. Lett. **76**, 1007.

[21] Bond, J.R., Efstathiou, G. & Tegmark, M. 1996, preprint.

[22] Knox, L. 1996, CITA preprint.

[23] Bond, J.R., Crittenden, J.R., Davis, R.L., Efstathiou, G. & Steinhardt, P.J. 1994, Phys. Rev. Lett. **72**, 13.